

Wide Binary Evaporation by Dark Solitons: Implications from the GAIA Catalog

Qiming Qiu^{1,*}, Yu Gao^{2,†}, Hai-jun Tian^{3,‡}, Kechen Wang^{4,§}, Zihang Wang^{2,¶} and Xiang-Ming Yang^{5,**}

¹*School of Physical Sciences, University of Chinese Academy of Sciences, 19A Yuquan Road, Beijing, China*

²*Key Laboratory of Particle Astrophysics, Institute of High Energy Physics, Chinese Academy of Sciences, Beijing 100049, China*

³*School of Science, Hangzhou Dianzi University, 310018 Hangzhou, Zhejiang, China*

⁴*Department of Physics, School of Science, Wuhan University of Technology, 430070 Wuhan, Hubei, China and College of Science, China Three Gorges University, Yichang 443002, People's Republic of China*

An analytic calculation is given for binary star evaporation under the tidal perturbation from randomly distributed, spatially extended dark objects. In particular, the Milky Way's wide binary star population are susceptible to such disruption from dark matter solitons of comparable and larger sizes. We identify high-probability 'halo-like' wide binaries in GAIA EDR3 with separations larger than 0.1 parsec. Survival of the farthest-separated candidates will provide a novel gravitational probe to dark matter in the form of solitons. In case of dilute axion-like solitons, the observational sensitivity is shown to extend into the axion mass range $m_a \sim 10^{-17} - 10^{-15}$ eV.

I. INTRODUCTION

Astrophysical observations indicate that cold dark matter composes a significant fraction of our Universe [1, 2]. Its gravity plays an important role in the formation of large-scale structures, galaxy clusters and galaxies themselves. Numerous models have been proposed, including weakly interacting particle candidates [3], macroscopic objects such as primordial black holes [4], exotic condensates [5, 6] and other MACHOs [7, 8] that typically behave as point particles on astrophysical scales. As one well-motivated scenario, ultralight dark matter [9, 10] predicts a more smooth density distribution and recently has gained strong interest, partially encouraged by issues at small scale [11]. In ultralight models, dark matter typically assumes the form of a low-mass scalar or pseudoscalar field. At a very low mass, the dark matter field's de Broglie wavelength is on astrophysical scales, naturally suppressing smaller-scale structures. Generally speaking, for low-mass dark matter, relatively small solitonic structures of boson stars [12, 13] and oscillons [14], such as axion miniclusters [15] clumps [16, 17], as well as denser variations [18, 19], can form via gravity and self-interaction, and make up the Galaxy's dark matter halo. Typically the very low scalar mass and the tiny interaction strength often make direct laboratory detection difficult. Astrophysical observations have played a major role, such as microlensing [20], pulsar timing [21, 22], radio emissions [23], etc. For solitons made of axion-like particles, which couple to photons, may generate fast radio bursts via stimulated decay [24–26] or conversion inside strong stellar magnetic fields [27–29].

Solitons are spatially extended objects, and they affect stellar motion gravitationally. Recent studies include star cluster relaxation [30–33], central galactic rotation curves [34], dynamic friction [35, 36] on galactic or dwarf galaxy scales. These scenarios typically consider a fuzzy dark matter that involves boson mass below 10^{-19} eV, and high-spin black hole superradiance exclusion limits apply a slightly higher boson mass range [37]. In principle, heavier bosons can also form solitons and leave their gravitational perturbations on smaller-scale objects. Noticeably our galaxy hosts a population of very wide binary star systems [38] with a separation up to 0.1 pc, around four orders of magnitude below the size of dwarf galaxies, and their vulnerability to external perturbation will offer a unique glance into similarly-sized dark solitons and correspondingly more massive bosons.

Tidal disruption of binaries has been a powerful tool to probe compact dark objects in close encounters [8]. Note there are also precision tests on Keplerian orbits on resonance with solitons in case the binary system contains pulsar(s) [39, 40]. In the case of dark solitons, they are spatially much more extended objects, and their tidal effects reveal only at scales larger than the boson field's coherence length. Thus the impact on stellar motion comes more gradually: The randomized tidal force from solitons will let the relative motion of the binary star gain energy slowly

*Electronic address: qiuqiming20@mails.ucas.ac.cn

†Electronic address: gaoyu@ihep.ac.cn

‡Electronic address: hjtian@hdu.edu.cn

§Electronic address: kechen.wang@whut.edu.cn

¶Electronic address: wangzihang@ihep.ac.cn

**Electronic address: xmyang@ctgu.edu.cn

and eventually evaporate away, which is in analog to the relaxation of star clusters yet on much smaller scales, plus a random walk in the binary's center of mass motion.

In this paper, we give a full calculation of the binary evaporation rate under the tidal disruption of spatially extended solitons. We construct the gravitational potential with three different soliton profiles in Section II and compute the evaporation rate in Section III. In Section IV we consider a selection of ‘halo-like’ wide binary candidates, which seem isolated from other stars in GAIA’s data. In Section V we illustrate the corresponding sensitivity limits from the survival of these binary catalogs and discuss their implication for axion-like solitons. Finally we summarize and conclude in Section VI.

II. POTENTIAL FROM SOLITONS

We will consider dark solitons or soliton-like structures as the main component of the dark matter halo. Well-motivated examples include the boson star [12, 17], in which quantum pressure, gravity and self-interaction balance each other and lead to an equilibrium configuration, and possess much higher densities compared to that of the background. These soliton’s mass and size will depend on the details of the interaction model, see Ref. [41] for recent reviews. In this work, we generally assume these solitons form, and we are interested in the situation that their non-negligible size becomes comparable or larger than the semi-major axis of the binary system’s orbit. The Milky Way’s observed binary systems can have a separation as far as 0.1 pc [38, 42]. This size can be achieved for solitons composed of ultralight bosons with $m_a \sim 10^{-17}$ eV. In contrast with binary disruption by point-like field stars [43], the density profile of the solitons must be taken into account, and their density fluctuations can be written as

$$\rho(\vec{x}, t) = \sum_i |\varphi(\vec{x} - \vec{x}_i - \vec{v}_i t)|^2 - \langle \rho \rangle, \quad (1)$$

where m_s is each soliton’s mass, φ is the normalized mass profile of the soliton, and \vec{x}_i, \vec{v}_i denote the location and velocity of soliton centers. For an individual soliton’s profile, we consider the case that φ is spherically symmetric. The density profile depends on the interaction model of the scalar field, and it can be obtained numerically. For simplicity, several analytical approximations of the density profile are often used. We will consider three parametrizations [17, 30]:

$$\varphi(r) = \begin{cases} \frac{m_s^{\frac{1}{2}}}{(2\pi R^2)^{\frac{3}{4}}} e^{-\frac{r^2}{4R^2}}, & \text{Gaussian;} \\ \left(\frac{3m_s}{\pi^3 R^3}\right)^{\frac{1}{2}} \text{sech}\left(\frac{r}{R}\right), & \text{Sech;} \\ \left(\frac{m_s}{7\pi R^3}\right)^{\frac{1}{2}} \left(1 + \frac{r}{R}\right) e^{-\frac{r}{R}}, & \text{Exponential linear (EL).} \end{cases} \quad (2)$$

where in each parametrization the scalar field is normalized so that the density of the scalar field satisfies $\rho(r) \propto \varphi(r)^2$. The parameter R is a characteristic radius of the profile. While R can be regarded as a boson star radius, the proportion of mass within radius R will vary between profiles. We assume that the mass and size are the same for all solitons, and show these profiles lead to comparable evaporation rates for binary stars.

The density distribution above can be rewritten into a correlation spectrum after Fourier transformation. Intuitively, a random spatial distribution of solitons will give a density correlation that resembles a short-noise on large scales ($k \ll R^{-1}$), which is similar to that with point-particles, but it develop structures at short scale $k \sim R^{-1}$ and eventually flattens out as $k \gg R^{-1}$, where the boson field is coherent. The two-point density correlation function is defined as

$$\langle \rho(\vec{r}, t) \rho(\vec{r}', t') \rangle \equiv C_\rho(\vec{r} - \vec{r}', t - t'). \quad (3)$$

Strictly speaking, we should subtract an average dark matter density ρ_0 here, i.e. $\rho(\vec{r}, t) = \rho_{\text{DM}}(\vec{r}, t) - \rho_0$, where $\rho_{\text{DM}}(\vec{r}, t)$ is the realistic dark matter density. The Fourier transformation of the correlation function is,

$$C_\rho(\vec{r}, t) = \int \frac{d^3 k d\omega}{(2\pi)^4} C_\rho(\vec{k}, \omega) e^{i(\vec{k} \cdot \vec{r} - \omega t)}. \quad (4)$$

Similarly the correlation function of the gravitational potential $\Phi(\vec{r}, t)$ is

$$\begin{aligned} \langle \Phi(\vec{r}, t) \Phi(\vec{r}', t') \rangle &\equiv C_\Phi(\vec{r} - \vec{r}', t - t'), \\ C_\Phi(\vec{r}, t) &= \int \frac{d^3 k d\omega}{(2\pi)^4} C_\Phi(\vec{k}, \omega) e^{i(\vec{k} \cdot \vec{r} - \omega t)}, \end{aligned}$$

and by Poisson's equation $\nabla^2\Phi = 4\pi G\rho$, they are related as $C_\Phi = 16\pi^2 G^2 k^{-4} C_\rho$. For soliton velocities, we include a Maxwellian distribution

$$F(\vec{v}) = \frac{\rho_0}{(2\pi\sigma^2)^{\frac{3}{2}}} e^{-\frac{v^2}{2\sigma^2}}. \quad (5)$$

where ρ_0 is the average dark matter density. The velocity distribution average [30] of $C_\rho(\vec{k}, \omega)$ takes the form

$$C_\rho(\vec{r}, t) = \frac{1}{m_s} \int d^3v d^3r' \rho(r') \rho(\vec{r} - \vec{r}' - \vec{v}t) F(\vec{v}). \quad (6)$$

After changing the integration variable, we obtain,

$$C_\rho(\vec{k}, \omega) = \frac{1}{m_s} \int d^3r d^3r' d^3v dt \rho(\vec{r}) \rho(\vec{r}') F(\vec{v}) e^{-i\vec{k}\cdot(\vec{r}+\vec{r}'+\vec{v}t)} e^{i\omega t}. \quad (7)$$

For Maxwellian velocity distribution Eq. (5), the expression above can be simplified,

$$C_\rho(\vec{k}, \omega) = \frac{1}{m_s} \rho^2(\vec{k}) \rho_0 \sqrt{\frac{2\pi}{k^2\sigma^2}} e^{-\frac{\omega^2}{2k^2\sigma^2}}. \quad (8)$$

where we have defined the Fourier transformation of $\rho(\vec{r})$,

$$\rho(\vec{k}) = \int d^3r \rho(\vec{r}) e^{-i\vec{k}\cdot\vec{r}}. \quad (9)$$

As long as the density profile of the soliton is known, we can calculate the correlation function and binary star evaporation rate in the section. In the following, we give the expressions of $\rho(\vec{k})$ and $C_\rho(\vec{k}, \omega)$ for different scalar field profiles. After performing the average, the correlation functions for the profiles are found to be

$$\begin{aligned} C_{\rho, \text{Gauss}}(\vec{k}, \omega) &= m_s \rho_0 \sqrt{\frac{2\pi}{k^2\sigma^2}} e^{-\frac{\omega^2}{2k^2\sigma^2}} e^{-k^2 R^2}, \\ C_{\rho, \text{Sech}}(\vec{k}, \omega) &= \frac{9m_s}{\pi^2 k^2 R^2} \left[-2 + \pi k R \coth\left(\frac{\pi k R}{2}\right) \right]^2 \text{csch}^2\left(\frac{\pi k R}{2}\right) \rho_0 \sqrt{\frac{2\pi}{k^2\sigma^2}} e^{-\frac{\omega^2}{2k^2\sigma^2}}, \\ C_{\rho, \text{EL}}(\vec{k}, \omega) &= \frac{4096m_s}{49} \frac{(28 + k^2 R^2)^2}{(4 + k^2 R^2)^8} \rho_0 \sqrt{\frac{2\pi}{k^2\sigma^2}} e^{-\frac{\omega^2}{2k^2\sigma^2}}. \end{aligned} \quad (10)$$

In the formulae above, time variance arises from both the relative motion between the binary system and the halo and that among the solitons themselves, and the latter averages out on large scales. For the binary's motion, we have $\omega \approx \vec{k} \cdot \vec{v}$. Therefore in the large scale limit $k \rightarrow 0$, where solitons appear to be point particles, one can verify $C_\rho \propto k^{-1}$, so that it will approach a noise spectrum, agreeing with classical calculations of compact objects. We will use these expressions to obtain the center of mass energy's growth rate in the next section.

III. EVAPORATION RATE

Denoting the velocities of the two stars relative to the dark matter background as \vec{v}_1 and \vec{v}_2 . The kinetic energy in center of mass frame is $E = \mu \vec{v}_r^2/2$, where μ is the reduced mass of the binary stars, and $\vec{v}_r = \vec{v}_1 - \vec{v}_2$ is the relative velocity between the two stars. An increment of energy in the center of mass frame of the binary star is

$$\Delta E = \mu \vec{v}_r \cdot \Delta \vec{v}_r + \frac{1}{2} \mu (\Delta \vec{v}_r)^2, \quad (11)$$

and the average growth rate over time T of is

$$\frac{\langle \Delta E \rangle}{T} = \mu \frac{\langle \vec{v}_r \cdot \Delta \vec{v}_r \rangle}{T} + \frac{1}{2} \mu \left(\frac{\langle \Delta \vec{v}_1^2 \rangle}{T} + \frac{\langle \Delta \vec{v}_2^2 \rangle}{T} - \frac{2\langle \Delta \vec{v}_1 \cdot \Delta \vec{v}_2 \rangle}{T} \right). \quad (12)$$

Here there are two averages: the $\langle \rangle$ brackets represent the average over the ensemble of potential variations, and the choice of T needs to account for the Keplerian period of the binary system. The large separation of wide binaries allows us to work in a 'slow orbit' limit,

$$\frac{\lambda_{\text{DM}}}{v} \ll T \ll \frac{2\pi}{\omega_b}, \quad (13)$$

which allows the ensemble average can be performed independently from that over T . λ_{DM} is the characteristic scale of the dark matter density fluctuations, v is the velocity of the binary star relative to the dark matter background, and ω_b is the orbital frequency. Consider a binary star with distance 0.1 pc and a total mass of $0.4M_\odot$, and the center of mass velocity at 200 km/s, slow orbit approximation requires $\lambda_{\text{DM}} \ll \text{kpc}$. For solitons with mass less than about $10^4 M_\odot$, the average distance between solitons is less than 10^2 pc. Hence the slow orbit approximation is generally satisfied for solitons in our interest.

The contribution from each term in Eq. 12 can be evaluated individually. Detailed calculations are listed in Appendix A, and here we only give the final results. The first $\vec{v}_r \cdot \langle \Delta \vec{v}_r \rangle$ term leads to

$$\frac{\vec{v}_r \cdot \langle \Delta \vec{v}_r \rangle}{T} = -\frac{1}{2} \int \frac{(\vec{k} \cdot \vec{v}_r) \vec{k}^2 d^3 k d\omega}{(2\pi)^3} C_\Phi(\vec{k}, \omega) \left(\delta'(\omega - \vec{k} \cdot \vec{v}_1) - \delta'(\omega - \vec{k} \cdot \vec{v}_2) \right), \quad (14)$$

Since $v_c \gg v_r$ and $v_1 \approx v_2 \approx v_c$, the integration over \vec{k} provides a $1/v_c$ factor. After integrating over directions of \vec{k} , the contribution from $\vec{v}_r \cdot \langle \Delta \vec{v}_r \rangle$ becomes suppressed by v_r/v_c . Besides, the $\vec{v}_r \cdot \langle \Delta \vec{v}_r \rangle$ term is further suppressed because the integration over \vec{k} direction contains cancellation positive and negative contributions. We find the contribution in Eq. 14 negligible compared to those from quadratic Δv terms.

The contribution from the others three terms in Eq. (12) take the form (see Appendix A)

$$\begin{aligned} \frac{\langle \Delta \vec{v}_1^2 \rangle}{T} &= \int \frac{\vec{k}^2 d^3 k}{(2\pi)^3} C_\Phi(\vec{k}, \vec{k} \cdot \vec{v}_1), \\ \frac{\langle \Delta \vec{v}_2^2 \rangle}{T} &= \int \frac{\vec{k}^2 d^3 k}{(2\pi)^3} C_\Phi(\vec{k}, \vec{k} \cdot \vec{v}_2) \\ \frac{\langle \Delta \vec{v}_1 \cdot \Delta \vec{v}_2 \rangle}{T} &= \int \frac{\vec{k}^2 d^3 k}{(2\pi)^3} C_\Phi(\vec{k}, \vec{k} \cdot \vec{v}_c) \cos[\vec{k} \cdot (\vec{r}_1 - \vec{r}_2)]. \end{aligned} \quad (15)$$

Note the last line in Eq. 15 uses the approximation $v_r \ll v_c$. After averaging the Maxwellian velocity distribution Eq. 5, the total energy growth rate is

$$\frac{\langle \Delta E \rangle}{T} = \sqrt{\frac{2}{\pi}} \frac{\mu \rho_0 G^2}{m_s \sigma} \int \frac{d^3 k}{k^3} \rho^2(\vec{k}) e^{-\frac{(\vec{k} \cdot \vec{v}_c)^2}{2k^2 \sigma^2}} 2 \left(1 - \cos \left[\vec{k} \cdot (\vec{r}_1 - \vec{r}_2) \right] \right). \quad (16)$$

The dependence on the soliton size is encoded in the cosine term, Intuitively, very small solitons would resemble point particles and their size should not matter; this is realized as the cosine term becomes highly oscillatory when $ka \gg 1$. In the large soliton limit, or $ka \ll 1$, the size dependence appears as $\sim (ka)^2$. Next, we integrate out the direction of \vec{k} and the above formula becomes

$$\frac{\langle \Delta E \rangle}{T} = \sqrt{\frac{2}{\pi}} \frac{\mu \rho_0 G^2}{m_s \sigma} \int_0^{+\infty} \frac{dk}{k} \rho^2(k) \int_{-1}^1 dx e^{-\frac{v_c^2 x^2}{2\sigma^2}} 4\pi \left[1 - J_0 \left(k \sqrt{r_x^2 + r_y^2} \sqrt{1 - x^2} \right) \cos(kr_z x) \right], \quad (17)$$

in which the relative position between the two stars is $\vec{r}_1 - \vec{r}_2 = (r_x, r_y, r_z)$ and we take the \hat{z} axis along \vec{v}_c direction. For easier comparison with a point-collision evaporation rate, we factor out the size and angle dependence,

$$\frac{\langle \Delta E \rangle}{T} = \left(\frac{\langle \Delta E \rangle}{T} \right)_0 A \left(r_x, r_y, r_z, R, \frac{v_c}{\sigma} \right). \quad (18)$$

where the forefactor is

$$\left(\frac{\langle \Delta E \rangle}{T} \right)_0 = \frac{8\pi \mu \rho_0 G^2 m_s}{v_c}. \quad (19)$$

The dimensionless function A can be evaluated for a fluctuation profile $\rho(k)$ of interest,

$$A = \frac{1}{\sqrt{2\pi}} \frac{v_c}{\sigma} \int_0^{+\infty} \frac{dk}{k} \frac{\rho^2(k)}{m_s^2} \int_{-1}^1 dx e^{-\frac{v_c^2 x^2}{2\sigma^2}} \left[1 - J_0 \left(k \sqrt{r_x^2 + r_y^2} \sqrt{1 - x^2} \right) \cos(kr_z x) \right], \quad (20)$$

where the inclination angle α denotes the angle between the normal vector of the orbital plane and \vec{v}_c . Fig. 1 illustrates the correction factor versus R/a for different soliton profiles (*left*) and different inclination angles (*right*), assuming circular binary star orbits. The three soliton profiles in Eq. 15 yield comparable evaporation rates. The curves turn

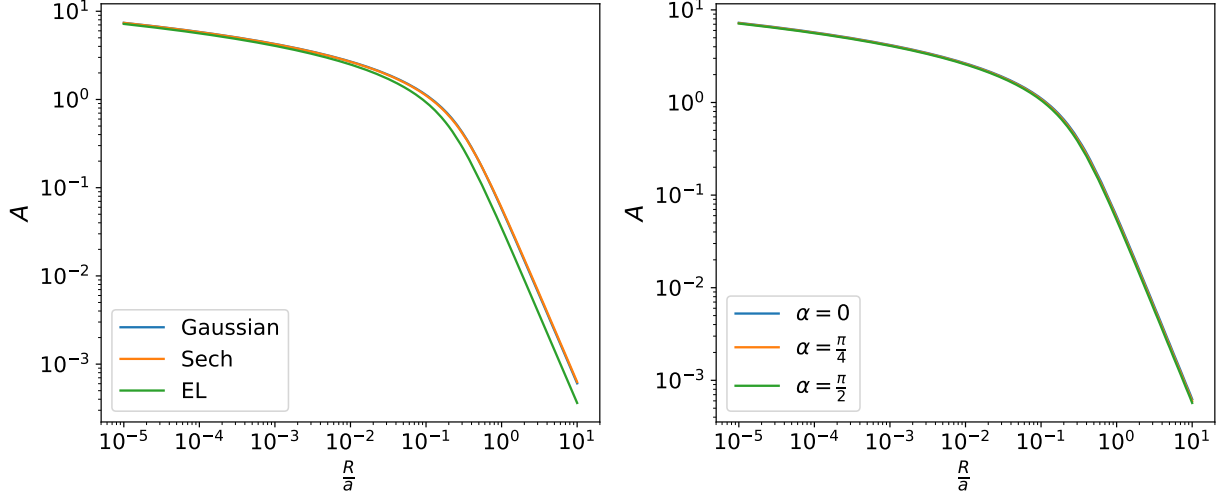


FIG. 1: The correction factor A dependence on R/a , where R is a characteristic radius of the soliton, a is the distance between the two stars. Here we take $v_c/\sigma = 1$ and we consider the circular orbit case. *Left*: A dependence on R/a for three different soliton profile. We are considering the case that \vec{v}_c is perpendicular to the orbital plane here, i.e. $\alpha = 0$. *Right*: R/a dependence at different inclination angles ($\alpha = 0, \pi/4, \pi/2$) with the ‘sech’ profile.

downward around $R/a \gtrsim 0.1$, indicating a more suppressed evaporation when the soliton size is comparable with or larger than that of the binary systems. The variation between profiles is partially due to the different definitions of R in the profiles. When changing inclination angle α , the evaporation rate only varies by around 10%, and the evaporation rate is higher at $\alpha = 0$ than at $\alpha = \pi/2$. Note this formula can be significantly simplified in the special case of $\alpha = 0$, or when \vec{v}_c is perpendicular to the orbital plane. If we further consider a circular orbit, namely $\sqrt{r_x^2 + r_y^2} \rightarrow a$, Eq. 20 will read

$$A\left(\frac{R}{a}, \frac{v_c}{\sigma}\right)\Big|_{\alpha=0, r \rightarrow a} = \frac{1}{\sqrt{2\pi}} \frac{v_c}{\sigma} \int_0^{+\infty} \frac{dk}{k} \frac{\rho^2(k)}{m_s^2} \int_{-1}^1 dx e^{-\frac{v_c^2 x^2}{2\sigma^2}} \left[1 - J_0\left(ka\sqrt{1-x^2}\right)\right]. \quad (21)$$

The evaporation time for a circular orbit can be obtained as

$$t_d = \int \frac{dE}{\langle \dot{E} \rangle} = \frac{|E_0|}{\left(\frac{dE}{dt}\right)_0} \int_0^1 \frac{du}{A\left(\frac{R}{a_0}u, \frac{v_c}{\sigma}\right)}, \quad (22)$$

where $u \equiv E_T/E_0$, a_0 is the initial distance between the two stars, $E_T = -GM_T\mu/2a$ is the sum of kinetic energy and potential energy, $E_0 = -\mu v_r^2/2$ is the initial total energy. We consider the evaporation as a gradual process, that E_T increases while the kinetic energy of the binary stars decreases as the separation a grows slowly. The first factor on the right-hand side can be regarded as a characteristic time scale,

$$t_{d0} \equiv \frac{|E_0|}{\left(\frac{dE}{dt}\right)_0} = \frac{v_r^2 v_c}{16\pi\rho_0 G^2 m_s} = \frac{v_c M_T}{16\pi\rho_0 G m_s a_0}. \quad (23)$$

where M_T is the total mass of the binary star, plus a numerical factor $B = \int_0^1 du / A\left(\frac{R}{a_0}u, \frac{v_c}{\sigma}\right)$ so that $t_d = t_{d0} \cdot B$. In Fig. 2 we plot B versus R/a_0 for different soliton profiles (*left*) and different inclination angle (*right*) for circular orbits. As would be expected, the evaporation time is longer when the solitons are more spatially extended, $R/a_0 \gtrsim \mathcal{O}(1)$. When comparing the disruption time with observations, one would need to average out the inclination angle. Assuming a uniform distribution of α , the evaporation time can be written as,

$$t_d = 6.6 \text{ Gyr} \left(\frac{v_r}{0.1 \text{ km/s}}\right)^2 \left(\frac{v_c}{200 \text{ km/s}}\right) \left(\frac{m_s}{30 M_\odot}\right)^{-1} \left(\frac{\rho_0}{0.4 \text{ GeV/cm}^3}\right)^{-1} B\left(\frac{R}{a_0}, \frac{v_c}{\sigma}\right), \quad (24)$$

or equivalently,

$$t_d = 14.3 \text{ Gyr} \left(\frac{M_T}{0.5 M_\odot}\right) \left(\frac{a_0}{0.1 \text{ pc}}\right)^{-1} \left(\frac{v_c}{200 \text{ km/s}}\right) \left(\frac{m_s}{30 M_\odot}\right)^{-1} \left(\frac{\rho_0}{0.4 \text{ GeV/cm}^3}\right)^{-1} B\left(\frac{R}{a_0}, \frac{v_c}{\sigma}\right). \quad (25)$$

This means that for low-mass binary stars with a large semi-major axis, solitons with $m_s \gtrsim \mathcal{O}(30)M_\odot$ in the dark matter halo can evaporate them over 10 billion years, which is in the same ballpark as the limits with MACHOs. Eq. 21-25 generalize the calculation to fluctuation profile $\rho(k)$, and readily apply to spatially extended objects like dark solitons. Here ρ_0 is the halo's dark matter density near the solar system, and in the rest of this paper we will assume solitons take up 100% of dark matter; in case soliton only make up a fraction of the density, t_d will scale inversely with this fraction.

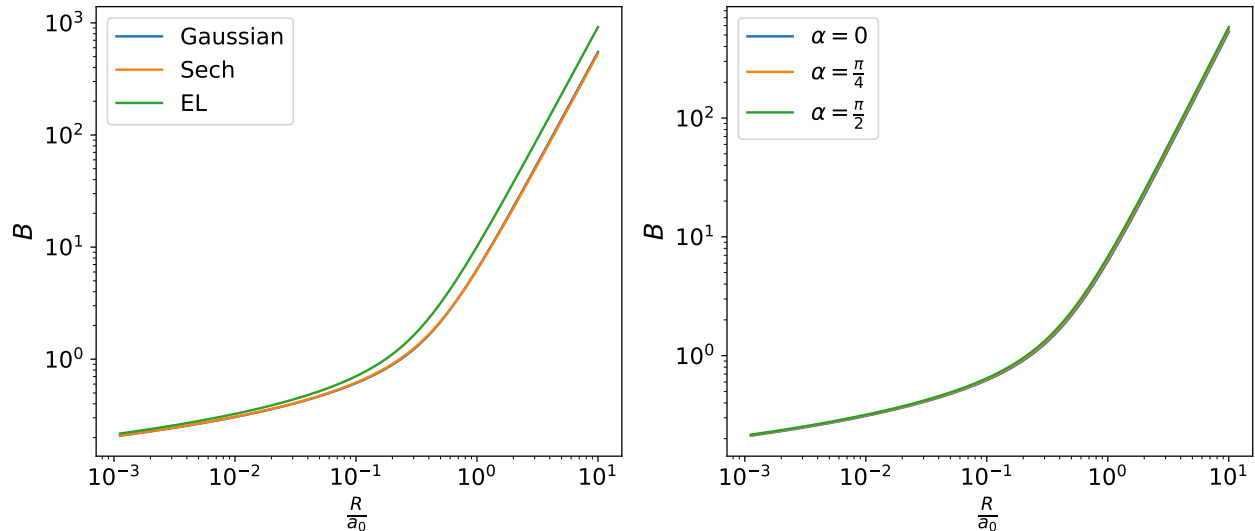


FIG. 2: The correction factor B for binary star evaporation time at soliton sizes. a_0 is the initial distance between the two stars. Here we take $v_c/\sigma = 1$ and consider circular orbits. *Left:* B dependence on R/a_0 for three different soliton profiles. We take inclination angle $\alpha = 0$. *Right:* B dependence on R/a_0 for inclination angle at $0, \pi/4$ and $\pi/2$ for the ‘sech’ profile.

IV. WIDE BINARY CANDIDATES

In this section we select binary candidates with the largest separation from GAIA data, to identify a population of the weakest binaries that are susceptible to dark boson stars’ tidal evaporation. We will start with the wide binary catalogue selected by Ref. [44] from the GAIA EDR3 dataset [45]. This catalogue encompasses 1,871,594 wide binary candidates. These systems reside within 1 kpc of the Sun, exhibit projected separations ranging from a few au to 1 pc, display similar proper motions consistent with a Keplerian orbit, and possess parallax measurements that align within a 3σ (or 6σ) for both components. The faked binary objects from clusters, background pairs and triples were effectively vetoed by removing the ones with either component having more than 30 neighbours. For the details on selection criteria of wide binaries, please refer to Section 2 in Ref. [46]. In the catalogue, two components of a wide binary system with the brighter and fainter GAIA G magnitude defined as the *primary* and *secondary* star, respectively.

We calculate the total tangential velocity with respect to the Sun for each candidate binary:

$$v_{\perp, \text{tot}} \equiv 4.74 \text{ km/s} \times (\mu_{\text{tot}} \times \text{yr}) / \varpi. \quad (26)$$

Here ϖ and $\mu_{\text{tot}} = \sqrt{\mu_{\alpha^*}^2 + \mu_\delta^2}$ are the parallax and total proper motion of a binary, respectively. As $v_{\perp, \text{tot}}$ can be considered as a proxy of binary system’s age, we select old halo-like binaries with the following criterion (see Ref. [47]),

$$v_{\perp, \text{tot}} > 85 \text{ km/s}. \quad (27)$$

To identify pure halo-like binary samples, we further impose the following cuts:

1. `R_chance_align` < 0.1 , approximately corresponding to a wide binary with $>90\%$ probability of being gravitationally bound. `R_chance_align` is evaluated in a seven-dimensional space [44] and it represents the probability that the two stars appear to be aligned by chance, a.k.a. ‘chance alignments’. High-probability binary candidates are expected to have low `R_chance_align` values.

2. $\text{ruwe}_1 < 1.4$ and $\text{ruwe}_2 < 1.4$. Here, the Renormalized Unit Weight Error (ruwe), a quality specified by the GAIA survey [48], indicates the binary system does not have another closer companion and has an apparently well-behaved astrometric solution.
3. The number of nearby neighbours $N < 2$, to strictly remove contaminants at wide separation from moving groups or star clusters.
4. We exclude binaries containing a white dwarf to remove the effect from internal orbital evolution.

With these cuts, we identify a collection of 62990 high-probability ($> 90\%$) halo-like binary candidates. As the dark matter’s tidal evaporation is more efficient for larger separation binaries, it is of interest to find out the binary population with the largest separation a_\perp . Within this collection, there are 2073 binaries with separation $0.1 < a_\perp < 0.5$ pc. When we require larger spatial separation, the count reduces to 13 for $0.5 < a_\perp < 0.7$ pc, and only 3 for $0.7 < a_\perp < 1$ pc. Here a_\perp denotes the projected separation. The mass-separation distribution of this binary collection is shown in Fig. 3.

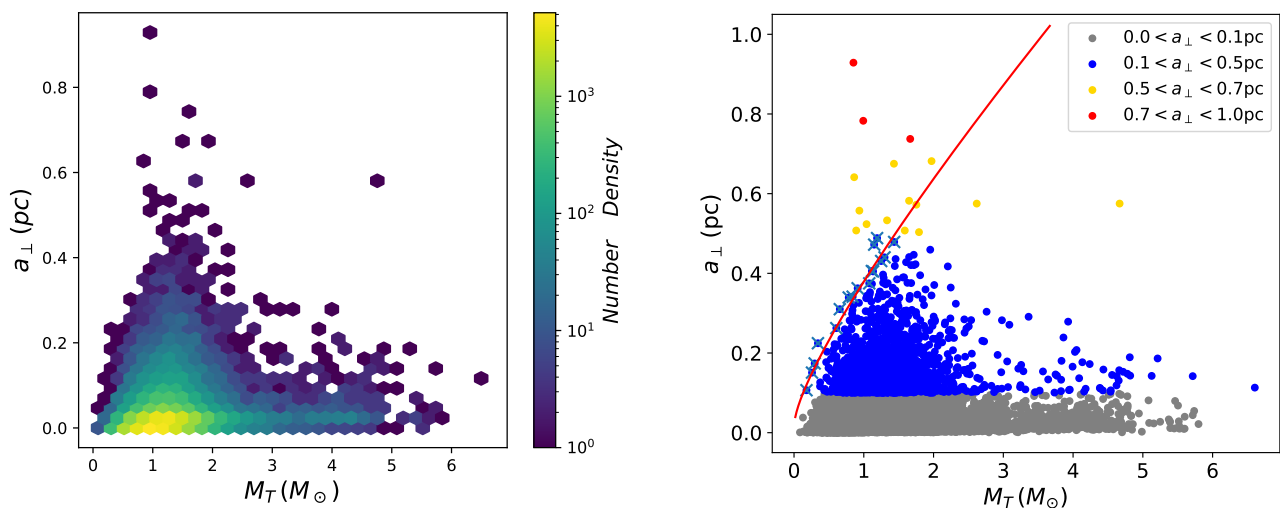


FIG. 3: The distribution of mass and projected separation of selected binaries. The left panel shows the population density. The right panel is color-coded by separation. The red curve running through the left edge of the populated region illustrates a tidal evaporation time of 10 Gyr by dark matter solitons with $m_s = 9.3 M_\odot$ and $R = 0.03$ pc, obtained from 17 boundary candidates (shown as \times) from Table III.

For halo-like binaries, a long lifetime is generally expected. It can be seen that the number of wide binaries decreases sharply for small total mass M_T and large separation a_\perp , which are easily disrupted by dark matter solitons. The sharp decrease of wide binaries is unlikely attributed to selection effects alone, which mainly reduce binaries with small M_T . As the formation mechanism for binaries at such a large separation is under ongoing research, here we do not go into depth with their astrophysical evolution, and satisfy with a proof-of-principle estimate by requiring dark matter perturbations do not significantly threaten the survival of such a population, namely by requiring $t_d < 10$ Gyr under dark matter perturbation. We can draw a $t_d = 10$ Gyr curve for given soliton mass and size, and a dark soliton scenario would become *disfavored* if large numbers of binaries are observed on the left side of its $t_d = 10$ Gyr curve.

Specifically, we selected 17 candidates with $0.1 < a_\perp < 0.5$ pc (see Appendix B), that represent the parameter space boundary where the number of binary stars decreases sharply. Their average $t_d = 10$ Gyr curve is illustrated by the red curve in the right panel of Fig. 3, corresponding to dark matter solitons with $m_s = 9.3 M_\odot$ and soliton radius $R = 0.03$ pc. Note our red curve is plotted by assuming random orientations of binary stars. Hence the projected separation a_\perp can be converted to the physical separation a using $a_\perp = (\pi/4)a$. This approximation is statistically suitable for randomly orientated systems.

The $t_d = 10$ Gyr curve marks out the region where dark matter’s tidal evaporation becomes significant. Nevertheless, the illustrated curve may not serve a clean-cut exclusion limit due to its statistical nature. Outliers can cross if they are more recently formed, or if they happen to have very elongated orbits. The exact location of the ‘boundary’ also depends on how stringent the selection cuts have been chosen. In what follows, we select two catalogs from

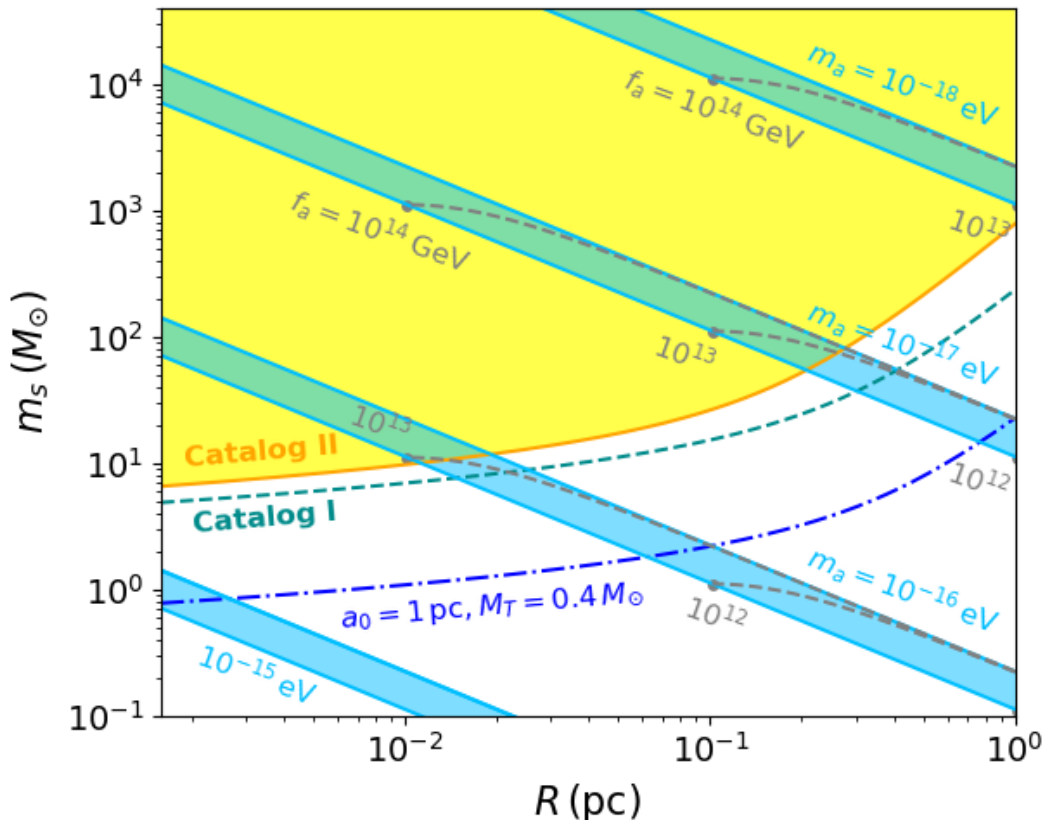


FIG. 4: Sensitivity to soliton mass and radius assuming ‘halo-like’ binary systems that survive 10 Gyr under tidal evaporation of dark matter in the form of dark solitons. The solid curve and dashed curve represent the limits from selected wide binaries in Catalog I and Catalog II. The dash-dot curve represents the constraint for binaries with $a_0 = 1$ pc and $M_T = 0.4 M_\odot$. The light-blue bands correspond to stable dilute axion star solutions with a fixed axion mass m_a while f_a is allowed to vary.

these binary candidates and use their average to represent the limits from a statistically significant halo-like binary population. For Catalog I, we include all the binaries with $a_\perp > 0.5$ pc and $M_T < 3 M_\odot$ after the selection cuts, and Catalog II will include all the wide binaries with $0.3 < a_\perp < 0.5$ pc and $M_T < 1.2 M_\odot$. Candidate details are listed in Table I and II of Appendix B. We will interpret their limits with soliton parameters in the next section.

V. RESULTS FOR ALP SOLITONS

We can place a limit on dark solitons by assuming the binary stars survive 10 Gyr. For a given soliton radius R , Eq. (25) yields a critical soliton mass m_s above which the average evaporation time,

$$\langle t_d \rangle \equiv \frac{1}{N} \sum_i t_{d,i} < 10 \text{ Gyr}, \quad i \text{ in each catalog.} \quad (28)$$

This means that the existence of solitons with mass above the critical mass will significantly affect the average lifetime of observed binary stars, hence the observed wide binaries provide rough constraints on soliton parameters. We plot constraints for soliton mass and radius in Fig. 4. The dashed cyan curve and solid orange curve are constraints from Catalog I and Catalog II, respectively. The yellow-shaded region of soliton parameter space is constrained by Catalog II, which contains fewer outliers, and can be considered as relatively conservative. Note there are a few candidates with $a \sim 1$ pc, it is uncertain whether these outliers truly represent a population of parsec-separation binaries, and we use a sample dot-dashed line ($a_0 = 1$ pc, $M_T = 0.4 M_\odot$) to show a projected 10 Gyr limit.

It is interesting to cast these limits into a particle physics model and see what boson mass range they are sensitive to. We consider the popular axion-like particles as a benchmark case, with an interaction potential $V(a) = m_a^2 f_a^2 [1 - \cos(a/f_a)]$ where m_a is the axion mass and f_a is the decay constant. For our purposes, there is no need to restrict to QCD origin so that the model parameters m_a, f_a are not tightly correlated. Such a soliton made of axion-like particles in gravitational equilibrium is often known as a dilute axion star, and its radius and total mass are determined by the number of bosons in the soliton solution. We use the rescaled radius $\tilde{R} = m_a f_a \sqrt{G} R$ and a rescaled particle number $\tilde{N} = m_a^2 N \sqrt{G} / f_a$. The rescaled radius $\tilde{R} = m_a f_a \sqrt{G} R$ is parametrized [17] as,

$$\tilde{R} = \frac{a \pm \sqrt{a^2 - 3bc\tilde{N}^2}}{b\tilde{N}}, \quad (29)$$

which adopts the ‘sech’ ansatz with $a = (12 + \pi^2)/6\pi^2$, $b = 6 [12\zeta(3) - \pi^2]/\pi^4$ and $c = (\pi^2 - 6)/8\pi^5$. ‘+’ sign corresponds to a stable configuration while ‘-’ sign is unstable. For a physical solution, it is required that $\tilde{N} < (a^2/3bc)^{1/2} \approx 10.12$. For a pair of axion parameters m_a and f_a , the configurations of dilute axion stars lie in a curve in the mass-radius diagram. If we fix the axion mass m_a and freely change f_a , the stable configurations lie in a blue band, as shown in Fig. 4 for different m_a . Generally, larger f_a allows solitons to contain more bosons and maintain a larger m_s . Dashed contours for different f_a values are shown inside each band. For instance, the $m_a = 10^{-17}$ eV band plotted in Fig. 4 corresponds to the f_a range around $10^{12} - 10^{15}$ GeV, and applies to models that derive the axionic potential from a high energy scale. The shaded region with Catalog II approximately corresponds to $f_a > 10^{13}$ GeV, and note this limit does not exclude large f_a as m_s can assume values below its maximum.

As the soliton size is typically inversely correlated with the axion boson mass, wide binary disruption limits become relevant for $m_a \gtrsim 10^{-18}$ eV, an axion mass range a few orders of magnitude higher than those from massive black hole superradiance and cluster relaxation limits [49]. Since tidal effects are gravitational, this axionic potential can be completely in the dark sector. The relevant f_a is not necessarily constrained by search limits that assume an axion coupling to the SM’s fermions or gauge fields. Admittedly, here we make the simplification that all dark matter solitons have like mass and size. The calculation with a non-trivial mass function will involve the evaluation of a distribution-weighted $\rho(k)$ in a particular model, and is of interest for future study.

VI. CONCLUSION

In summary, we have calculated the tidal evaporation of slow-rotating, wide-separation two-body systems under the gravitational perturbation from randomly distributed and spatially extended objects. The effect from the object’s profile and its characteristic scale can be analytically accounted for in a concise form by Eq. 16. We find the evaporation disruption on the Galaxy’s wide binaries particularly interesting for dark matter solitons of a comparable granularity scale to binary separations. The result can also apply to other tidal perturbations with a given spectrum that returns to noise over large scales. Non-stochastic tidal effects, like those from the central gravitational field of a host halo, would still need to be accounted for separately.

We selected high-probability halo-like binary candidates with separation larger than 0.1 parsec from the recent GAIA EDR3 set. More than two thousand candidates pass our selection cuts. We selected two catalogs of promising candidates in Catalog I and II, containing the ones with the largest separation ($a_\perp > 0.5$ pc), and less massive candidates ($M_T < 1.2M_\odot$ and $0.3 < a_\perp < 0.5$ pc). For isolated halo-like binary systems, their disruption should be dominated by dark matter substructures in the halo. Assuming an evaporation time longer than 10 Gyr, the survival of these halo-like binary populations can provide a scale-dependent limit on dark matter in the form of solitons.

Soliton-like structures are common in various low-mass bosonic dark matter models. For solitons with size smaller than $\mathcal{O}(\text{pc})$ and mass larger than a few solar masses, they will start to disrupt wide binaries in a significant way. We adopt several typical ansatzes for axion-like particle solitons to interpret the halo-like binary disruption into the physical model. As would be expected from the inverse correlation between the dark matter particle mass and its soliton granularity scale, our GAIA binary catalogs’ limits are sensitive to a more massive range of the ALP boson, around $m_a = 10^{-17} - 10^{-15}$ eV, higher than the existing constraints from massive black holes and star clusters, and the relevant f_a range is above 10^{13} GeV.

Due to its gravitational nature, the tidal effect from dark matter does not require direct coupling between the dark and the Standard Model sectors, thus wide binaries provide an interesting observation window on dark density granularity around the parsec scale. Similar disruption may also appear for other weakly bound systems, e.g. early stage of gravitational capture between celestial objects, etc.

Acknowledgements.

The authors thank Scott Tremaine for helpful communications. This work is supported in part by the National

Natural Science Foundation of China (No. 12275278, 12150010 and 12373033). Q. Qiu acknowledges support from the University of Chinese Academy of Sciences and the Institute of High Energy Physics, Chinese Academy of Sciences (No. KCJH-80009-2022-14).

-
- [1] Y. Akrami et al. (Planck), *Astron. Astrophys.* **641**, A10 (2020), 1807.06211.
- [2] M. Markevitch, A. H. Gonzalez, D. Clowe, A. Vikhlinin, L. David, W. Forman, C. Jones, S. Murray, and W. Tucker, *Astrophys. J.* **606**, 819 (2004), astro-ph/0309303.
- [3] A. Boveia et al. (2022), 2211.07027.
- [4] B. J. Carr and S. W. Hawking, *Mon. Not. Roy. Astron. Soc.* **168**, 399 (1974).
- [5] J. Madsen, H. Heiselberg, and K. Riisager, *Phys. Rev. D* **34**, 2947 (1986).
- [6] M. Hindmarsh, *Phys. Rev. D* **45**, 1130 (1992).
- [7] A. Gould, *Astrophys. J. Lett.* **421**, L71 (1994).
- [8] J. Yoo, J. Chaname, and A. Gould, *Astrophys. J.* **601**, 311 (2004), astro-ph/0307437.
- [9] J. P. Hui, Lam pand Ostriker, S. Tremaine, and E. Witten, *Phys. Rev. D* **95**, 043541 (2017), 1610.08297.
- [10] M. S. Turner, *Phys. Rev. D* **28**, 1243 (1983).
- [11] D. H. Weinberg, J. S. Bullock, F. Governato, R. Kuzio de Naray, and A. H. G. Peter, *Proc. Nat. Acad. Sci.* **112**, 12249 (2015), 1306.0913.
- [12] P. Jetzer, *Phys. Rept.* **220**, 163 (1992).
- [13] P. S. Wesson, *Astrophys. J. Lett.* **420**, L49 (1994).
- [14] E. Seidel and W. M. Suen, *Phys. Rev. Lett.* **66**, 1659 (1991).
- [15] S. Chang, C. Hagmann, and P. Sikivie, *Phys. Rev. D* **59**, 023505 (1999), hep-ph/9807374.
- [16] A. H. Guth, M. P. Hertzberg, and C. Prescod-Weinstein, *Phys. Rev. D* **92**, 103513 (2015), 1412.5930.
- [17] E. D. Schiappacasse and M. P. Hertzberg, *JCAP* **01**, 037 (2018), [Erratum: *JCAP* 03, E01 (2018)], 1710.04729.
- [18] E. Braaten, A. Mohapatra, and H. Zhang, *Phys. Rev. Lett.* **117**, 121801 (2016), 1512.00108.
- [19] L. Visinelli, S. Baum, J. Redondo, K. Freese, and F. Wilczek, *Phys. Lett. B* **777**, 64 (2018), 1710.08910.
- [20] M. Fairbairn, D. J. E. Marsh, J. Quevillon, and S. Rozier, *Phys. Rev. D* **97**, 083502 (2018), 1707.03310.
- [21] J. A. Dror, H. Ramani, T. Trickle, and K. M. Zurek, *Phys. Rev. D* **100**, 023003 (2019), 1901.04490.
- [22] H. Ramani, T. Trickle, and K. M. Zurek, *JCAP* **12**, 033 (2020), 2005.03030.
- [23] I. I. Tkachev, *JETP Lett.* **101**, 1 (2015), 1411.3900.
- [24] M. P. Hertzberg and E. D. Schiappacasse, *JCAP* **11**, 004 (2018), 1805.00430.
- [25] A. Arza, *Eur. Phys. J. C* **79**, 250 (2019), 1810.03722.
- [26] Z. Wang, L. Shao, and L. X. Li, *JCAP* **07**, 038 (2020), 2002.09144.
- [27] A. Iwazaki, *Phys. Rev. D* **91**, 023008 (2015), 1410.4323.
- [28] J. H. Buckley, P. S. B. Dev, F. Ferrer, and F. P. Huang, *Phys. Rev. D* **103**, 043015 (2021), 2004.06486.
- [29] R. A. Battye, B. Garbrecht, J. I. McDonald, F. Pace, and S. Srinivasan, *Phys. Rev. D* **102**, 023504 (2020), 1910.11907.
- [30] B. Bar-Or, J.-B. Fouvry, and S. Tremaine, *Astrophys. J.* **871**, 28 (2019), 1809.07673.
- [31] D. J. E. Marsh and J. C. Niemeyer, *Phys. Rev. Lett.* **123**, 051103 (2019), 1810.08543.
- [32] A. Wasserman, P. van Dokkum, A. J. Romanowsky, J. Brodie, S. Danieli, D. A. Forbes, R. Abraham, C. Martin, M. Matuzewski, A. Villaume, et al., *The Astrophysical Journal* **885**, 155 (2019), 1905.10373.
- [33] J. C. Niemeyer, *Progress in Particle and Nuclear Physics* **113**, 103787 (2019), 1912.07064.
- [34] N. Bar, K. Blum, J. Eby, and R. Sato, *Phys. Rev. D* **99**, 103020 (2019), 1903.03402.
- [35] Y. Wang and R. Easther, *Phys. Rev. D* **105**, 063523 (2022), 2110.03428.
- [36] R. Buehler and V. Desjacques, *Phys. Rev. D* **107**, 023516 (2023), 2207.13740.
- [37] A. Arvanitaki, M. Baryakhtar, and X. Huang, *Phys. Rev. D* **91**, 084011 (2015), 1411.2263.
- [38] H.-J. Tian, K. El-Badry, H.-W. Rix, and A. Gould, *The Astrophysical Journal Supplement Series* **246**, 4 (2019), ISSN 1538-4365, URL <http://dx.doi.org/10.3847/1538-4365/ab54c4>.
- [39] D. Blas, D. López Nacir, and S. Sibiryakov, *Phys. Rev. D* **101**, 063016 (2020), 1910.08544.
- [40] J. M. Armaleo, D. López Nacir, and F. R. Urban, *JCAP* **01**, 053 (2020), 1909.13814.
- [41] L. Visinelli, *Int. J. Mod. Phys. D* **30**, 2130006 (2021), 2109.05481.
- [42] J. Peñarrubia, A. D. Ludlow, J. Chanamé, and M. G. Walker, *Mon. Not. Roy. Astron. Soc.* **461**, L72 (2016), 1605.09384.
- [43] J. Binney and S. Tremaine, *Galactic Dynamics* (Princeton University Press, 2008).
- [44] K. El-Badry, H.-W. Rix, and T. M. Heintz, *Mon. Not. Roy. Astron. Soc.* **506**, 2269 (2021), 2101.05282.
- [45] Gaia Collaboration, S. A. Klioner, F. Mignard, L. Lindgren, U. Bastian, P. J. McMillan, J. Hernández, D. Hobbs, M. Ramos-Lerate, M. Biermann, et al., *Astronomy & Astrophysics* **649**, A9 (2021), 2012.02036.
- [46] K. El-Badry and H.-W. Rix, *Mon. Not. Roy. Astron. Soc.* **480**, 4884 (2018), 1807.06011.
- [47] H.-J. Tian, K. El-Badry, H.-W. Rix, and A. Gould, *The Astrophysical Journal Supplement Series* **246**, 4 (2020), 1909.04765.
- [48] C. Fabricius, X. Luri, F. Arenou, C. Babusiaux, A. Helmi, T. Muraveva, C. Reylé, F. Spoto, A. Vallenari, T. Antoja, et al., *Astronomy & Astrophysics* **649**, A5 (2021), 2012.06242.
- [49] D. Antypas et al. (2022), 2203.14915.

Appendix A: Slow orbits

Here we derive the evaporation effect from density fluctuations on a slowly rotating binary system. Namely, the binary rotation period is slow compared to the time scale of gravitational perturbations. This requires

$$\frac{\lambda_{\text{DM}}}{v} \ll T \ll \frac{2\pi}{\omega_b}, \quad (\text{A1})$$

where λ_{DM} is the characteristic scale of the dark matter density fluctuations, v is the velocity of the binary star relative to the dark matter background, ω_b is the orbital frequency, T is a time interval during which we ensemble average over gravitational perturbations. \vec{v}_1 and \vec{v}_2 are the velocities of the two stars relative to the dark matter halo. With the slow orbit approximation, we will treat the position and the velocity in the binary's relative motion as constants before averaging over the gravitational potential Φ . The orbital kinetic energy in the center of mass frame is, $E = \mu \vec{v}_r^2/2$, where μ is the reduced mass of the binary stars, $\vec{v}_r = \vec{v}_1 - \vec{v}_2$ is the relative velocity of the two stars. First, we briefly review the essential definitions for a generic calculation with randomized forces. The Fourier transformation of the gravitational potential is

$$\Phi(\vec{r}, t) = \int \frac{d^3k d\omega}{(2\pi)^4} \Phi(\vec{k}, \omega) e^{i(\vec{k} \cdot \vec{r} - \omega t)}. \quad (\text{A2})$$

The correlation function in coordinate space is,

$$\langle \Phi(\vec{r}, t) \Phi(\vec{r}', t') \rangle = C_\Phi(\vec{r} - \vec{r}', t - t') \quad (\text{A3})$$

which is a real-valued function. Its Fourier transformation is,

$$C_\Phi(\vec{k}, \omega) = \int d^3r dt C_\Phi(\vec{r}, t) e^{-i\vec{k} \cdot \vec{r} - i\omega t}. \quad (\text{A4})$$

Making use of the relation $C_\Phi(\vec{k}, \omega) = C_\Phi^*(-\vec{k}, -\omega)$ and from Eq. (A2)(A3)(A4) we obtain

$$\langle \Phi(\vec{k}, \omega) \Phi^*(\vec{k}', \omega') \rangle = (2\pi)^4 C_\Phi(\vec{k}, \omega) \delta^3(\vec{k} - \vec{k}') \delta(\omega - \omega'). \quad (\text{A5})$$

One would need to expand the binary's spatial motion through the fluctuating background. The position of a star $\vec{r}(t)$ can be written with the initial position \vec{r}_0 and velocity \vec{v}_0 ,

$$\vec{r}(t) \approx \vec{r}_0 + \vec{v}_0 t + \int_0^t ds (t-s) \dot{\vec{v}}(s), \quad (\text{A6})$$

and the acceleration due to the gravitational potential is

$$\dot{\vec{v}}(\vec{r}, t) = -\nabla \Phi(\vec{r}, t) = -i \int \frac{\vec{k} d^3k d\omega}{(2\pi)^4} \Phi(\vec{k}, \omega) e^{i(\vec{k} \cdot \vec{r} - \omega t)}, \quad (\text{A7})$$

and the change of velocity after a time interval T is,

$$\Delta \vec{v} = -i \int_0^T dt \int \frac{\vec{k} d^3k d\omega}{(2\pi)^4} \Phi(\vec{k}, \omega) e^{i(\vec{k} \cdot \vec{r} - \omega t)}. \quad (\text{A8})$$

Using Eq. (A6), the exponential factor is further expanded into

$$\begin{aligned} \exp \left[i(\vec{k} \cdot \vec{r} - \omega t) \right] &= \exp \left[i\vec{k} \cdot \left(\vec{r}_0 + \vec{v}_0 t + \int_0^t d\tau (t-\tau) \dot{\vec{v}}(\vec{r}_0 + \vec{v}_0 \tau, \tau) \right) - i\omega t \right] \\ &\approx e^{i\vec{k} \cdot (\vec{r}_0 + \vec{v}_0 t) - i\omega t} \left[1 + i\vec{k} \cdot \int_0^t d\tau (t-\tau) \dot{\vec{v}}(\vec{r}_0 + \vec{v}_0 \tau, \tau) \right], \end{aligned} \quad (\text{A9})$$

in which the first term (unity) in the square brackets does not contribute to the first order diffusion coefficient $\langle \Delta v \rangle / T$, because $\Phi(\vec{k}, \omega)$ averages to zero during the ensemble average. Contribution only comes from the second term:

$$\Delta \vec{v} = i \int_0^T dt \int_0^t d\tau (t-\tau) \int \frac{\vec{k} d^3k d\omega}{(2\pi)^4} \int \frac{(\vec{k} \cdot \vec{k}') d^3k' d\omega'}{(2\pi)^4} \Phi(\vec{k}, \omega) \Phi^*(\vec{k}', \omega') e^{i\vec{k} \cdot (\vec{r}_0 + \vec{v}_0 t) - i\omega t} e^{-i\vec{k}' \cdot (\vec{r}_0 + \vec{v}_0 \tau) + i\omega' \tau}. \quad (\text{A10})$$

Performing the ensemble average and use Eq. (A5), we obtain

$$\begin{aligned} \langle \Delta \vec{v} \rangle &= i \int_0^T dt \int_0^t d\tau (t - \tau) \int \frac{\vec{k} d^3 k d\omega}{(2\pi)^4} \vec{k}^2 C_\Phi(\vec{k}, \omega) e^{i\vec{k} \cdot (\vec{r}_0 + \vec{v}_0 t) - i\omega t} e^{-i\vec{k} \cdot (\vec{r}_0 + \vec{v}_0 \tau) + i\omega \tau} \\ &= \int_0^T dt \int_0^t d\tau \int \frac{d^3 k d\omega}{(2\pi)^4} \vec{k}^2 C_\Phi(\vec{k}, \omega) \frac{\partial}{\partial v_0} e^{i(\vec{k} \cdot \vec{v}_0 - \omega)(t - \tau)}. \end{aligned} \quad (\text{A11})$$

By interchanging the integration over t and τ , and using the fact that $\Delta \vec{v}, C_\Phi(\vec{k}, \omega)$ being real, this formula can be rewritten as

$$\langle \Delta \vec{v} \rangle = \frac{1}{2} \int_0^T dt \int_0^T d\tau \int \frac{d^3 k d\omega}{(2\pi)^4} \vec{k}^2 C_\Phi(\vec{k}, \omega) \frac{\partial}{\partial v_0} e^{i(\vec{k} \cdot \vec{v}_0 - \omega)(t - \tau)} \quad (\text{A12})$$

Using the notation in Ref. [30],

$$K_T(\omega) = \frac{1}{2\pi T} \int_0^T ds \int_0^T ds' e^{i\omega(s-s')} = \frac{1 - \cos(\omega T)}{\pi \omega^2 T}, \quad (\text{A13})$$

and its derivative

$$K_T'(\omega) = \frac{\omega T \sin(\omega T) - 2[1 - \cos(\omega T)]}{\pi \omega^3 T}, \quad (\text{A14})$$

we can rewrite Eq. A12 into

$$D[\Delta \vec{v}] = \frac{\langle \Delta \vec{v} \rangle}{T} = -\frac{1}{2} \int \frac{\vec{k} d^3 k d\omega}{(2\pi)^3} \vec{k}^2 C_\Phi(\vec{k}, \omega) K_T'(\omega - \vec{k} \cdot \vec{v}_0). \quad (\text{A15})$$

For readers familiar with diffusion calculations, this is the first-order Fokker-Planck coefficient. At this point, we are now ready to apply this formalism to binary star evaporation.

For a binary system, $\Delta \vec{v}_r = \Delta \vec{v}_1 - \Delta \vec{v}_2$. Repeat the process above and we will obtain

$$\frac{\vec{v}_r \cdot \langle \Delta \vec{v}_r \rangle}{T} = -\frac{1}{2} \int \frac{(\vec{k} \cdot \vec{v}_r) \vec{k}^2 d^3 k d\omega}{(2\pi)^3} C_\Phi(\vec{k}, \omega) \left(K_T'(\omega - \vec{k} \cdot \vec{v}_1) - K_T'(\omega - \vec{k} \cdot \vec{v}_2) \right). \quad (\text{A16})$$

As energy increment contains terms with products of Δv , we also need to compute second-order diffusion coefficients. The calculation process is very similar. We use Eq. (A8) and Eq. (A9), but now we only need the unity term inside the brackets in Eq. (A9). We consider $\langle \Delta v_i \Delta v_j \rangle$ first, where $\Delta \vec{v}$ is the velocity change of a star under gravitational perturbations and $i, j \in \{x, y, z\}$ are spatial components of $\Delta \vec{v}$:

$$\Delta v_i \Delta v_j = \int_0^T ds \int_0^T ds' \int \frac{k_i d^3 k d\omega}{(2\pi)^4} \int \frac{k'_j d^3 k' d\omega'}{(2\pi)^4} \Phi(\vec{k}, \omega) \Phi^*(\vec{k}', \omega') e^{i\vec{k} \cdot (\vec{r}_0 + \vec{v}_0 s) - i\omega s} e^{-i\vec{k}' \cdot (\vec{r}_0 + \vec{v}_0 s') + i\omega' s'}, \quad (\text{A17})$$

$$\langle \Delta v_i \Delta v_j \rangle = \int \frac{k_i k_j d^3 k d\omega}{(2\pi)^4} \int_0^T ds \int_0^T ds' C_\Phi(\vec{k}, \omega) e^{i(\vec{k} \cdot \vec{v}_0 - \omega)(s - s')}, \quad (\text{A18})$$

$$\text{and } \frac{\langle \Delta v_i \Delta v_j \rangle}{T} = \int \frac{k_i k_j d^3 k d\omega}{(2\pi)^3} C_\Phi(\vec{k}, \omega) K_T(\omega - \vec{k} \cdot \vec{v}_0). \quad (\text{A19})$$

So that

$$\begin{aligned} \frac{\langle \Delta \vec{v}_1^2 \rangle}{T} &= \int \frac{\vec{k}^2 d^3 k d\omega}{(2\pi)^3} C_\Phi(\vec{k}, \omega) K_T(\omega - \vec{k} \cdot \vec{v}_1), \\ \frac{\langle \Delta \vec{v}_2^2 \rangle}{T} &= \int \frac{\vec{k}^2 d^3 k d\omega}{(2\pi)^3} C_\Phi(\vec{k}, \omega) K_T(\omega - \vec{k} \cdot \vec{v}_2), \end{aligned} \quad (\text{A20})$$

and for the $\Delta v_1 \Delta v_2$ term,

$$\Delta v_{1i} \Delta v_{2j} = \int_0^T ds \int_0^T ds' \int \frac{k_i d^3 k d\omega}{(2\pi)^4} \int \frac{k'_j d^3 k' d\omega'}{(2\pi)^4} \Phi(\vec{k}, \omega) \Phi^*(\vec{k}', \omega') e^{i\vec{k} \cdot (\vec{r}_1 + \vec{v}_1 s) - i\omega s} e^{-i\vec{k}' \cdot (\vec{r}_2 + \vec{v}_2 s') + i\omega' s'}. \quad (\text{A21})$$

Taking the ensemble average (Eq. A5), we obtain

$$\langle \Delta v_{1i} \Delta v_{2j} \rangle = \int \frac{k_i k_j d^3 k d\omega}{(2\pi)^4} e^{i\vec{k} \cdot (\vec{r}_1 - \vec{r}_2)} C_\Phi(\vec{k}, \omega) \int_0^T ds \int_0^T ds' e^{-i(\omega - \vec{k} \cdot \vec{v}_1) s} e^{i(\omega - \vec{k} \cdot \vec{v}_2) s'}, \quad (\text{A22})$$

$$\frac{\langle \Delta \vec{v}_1 \cdot \Delta \vec{v}_2 \rangle}{T} = \int \frac{\vec{k}^2 d^3 k d\omega}{(2\pi)^4} C_\Phi(\vec{k}, \omega) \frac{e^{i\vec{k} \cdot (\vec{r}_1 - \vec{r}_2)}}{T} \frac{e^{-i(\omega - \vec{k} \cdot \vec{v}_1) T} - 1}{\omega - \vec{k} \cdot \vec{v}_1} \frac{e^{i(\omega - \vec{k} \cdot \vec{v}_2) T} - 1}{\omega - \vec{k} \cdot \vec{v}_2}. \quad (\text{A23})$$

To proceed further analytically, we consider a simplification with $v_1 \approx v_2 \approx v_c$ since the center of mass velocity is much larger than that of the relative motion, $v_c \gg v_r$. For the binary star we considered here, $v_c \sim 200$ km/s and $v_r \lesssim 1$ km/s, and this condition is satisfied. Eq. A23 then becomes

$$\frac{\langle \Delta \vec{v}_1 \cdot \Delta \vec{v}_2 \rangle}{T} = \int \frac{\vec{k}^2 d^3 k d\omega}{(2\pi)^3} C_\Phi(\vec{k}, \omega) e^{i\vec{k} \cdot (\vec{r}_1 - \vec{r}_2)} K_T(\omega - \vec{k} \cdot \vec{v}_c). \quad (\text{A24})$$

Note by interchanging $1 \leftrightarrow 2$, the exponential factor $e^{i\vec{k} \cdot (\vec{r}_1 - \vec{r}_2)} \leftrightarrow e^{-i\vec{k} \cdot (\vec{r}_1 - \vec{r}_2)}$. One can verify that

$$\frac{\langle \Delta \vec{v}_1 \cdot \Delta \vec{v}_2 \rangle}{T} = \int \frac{\vec{k}^2 d^3 k d\omega}{(2\pi)^3} C_\Phi(\vec{k}, \omega) \cos[\vec{k} \cdot (\vec{r}_1 - \vec{r}_2)] K_T(\omega - \vec{k} \cdot \vec{v}_c). \quad (\text{A25})$$

The total growth rate of energy in the center of mass frame is

$$\frac{\langle \Delta E \rangle}{T} = \mu \frac{\vec{v}_r \cdot \langle \Delta \vec{v}_r \rangle}{T} + \frac{1}{2} \mu \left(\frac{\langle \Delta \vec{v}_1^2 \rangle}{T} + \frac{\langle \Delta \vec{v}_2^2 \rangle}{T} - \frac{2 \langle \Delta \vec{v}_1 \cdot \Delta \vec{v}_2 \rangle}{T} \right). \quad (\text{A26})$$

Using $K_T(\omega) \rightarrow \delta(\omega)$ for large T , we can finally write down the expression for each term:

$$\frac{\vec{v}_r \cdot \langle \Delta \vec{v}_r \rangle}{T} = -\frac{1}{2} \int \frac{(\vec{k} \cdot \vec{v}_r) \vec{k}^2 d^3 k d\omega}{(2\pi)^3} C_\Phi(\vec{k}, \omega) \left(\delta'(\omega - \vec{k} \cdot \vec{v}_1) - \delta'(\omega - \vec{k} \cdot \vec{v}_2) \right), \quad (\text{A27})$$

$$\frac{\langle \Delta \vec{v}_1^2 \rangle}{T} = \int \frac{\vec{k}^2 d^3 k}{(2\pi)^3} C_\Phi(\vec{k}, \vec{k} \cdot \vec{v}_1), \quad (\text{A28})$$

$$\frac{\langle \Delta \vec{v}_2^2 \rangle}{T} = \int \frac{\vec{k}^2 d^3 k}{(2\pi)^3} C_\Phi(\vec{k}, \vec{k} \cdot \vec{v}_2), \quad (\text{A29})$$

$$\frac{\langle \Delta \vec{v}_1 \cdot \Delta \vec{v}_2 \rangle}{T} = \int \frac{\vec{k}^2 d^3 k}{(2\pi)^3} C_\Phi(\vec{k}, \vec{k} \cdot \vec{v}_c) \cos[\vec{k} \cdot (\vec{r}_1 - \vec{r}_2)]. \quad (\text{A30})$$

Appendix B: Wide binary catalogs

Here we list wide binary catalogs used in Section V. Table I contains the ‘Catalog I’ candidates with $a_\perp > 0.5$ pc and $M_T < 3 M_\odot$, shown in orange and red colors in the right panel of Fig. 3. Table II contains the relatively low-mass candidates with $0.3 < a_\perp < 0.5$ pc and $M_T < 1.2 M_\odot$. All candidates pass our selection cuts with their $R_{\text{chance align}} < 0.1$. Table III contains 17 on-boundary candidates we adopted to produce the $t_d = 10$ Gyr curve in Fig. 3. The data used for selection are available from Ref. [44] and data source therein: <https://zenodo.org/records/4435257>.

Source id1	Source id2	parallax1	parallax2	g mag1	g mag2	R chance align	M_1	M_2	M_T	a_{\perp} (pc)
1312689344512158848	1312737894822499968	3.375	3.310	12.07	17.21	0.000996	0.950	0.483	1.432	0.675
6644959785879883776	6644776515331203840	2.007	2.354	17.85	18.00	0.0462	0.440	0.412	0.851	0.929
2305945096292235648	2305945538674043392	2.366	2.316	15.74	17.30	1.53e-09	0.518	0.373	0.891	0.508
2127864001174217088	2127863726296352256	1.370	1.363	13.64	15.60	0.0357	0.924	0.741	1.665	0.737
577970351704355072	580975626220823296	3.117	3.021	16.35	17.47	0.0850	0.484	0.452	0.937	0.557
1401312283813377536	1401310698969746944	1.244	1.234	16.97	18.92	0.0113	0.631	0.409	1.040	0.523
1559537092292382720	1559533965556190848	1.209	1.224	13.63	15.03	0.00142	1.117	0.854	1.971	0.682
5476416420063651840	5476421406528047104	1.204	1.214	13.66	15.46	0.0834	1.016	0.775	1.791	0.503
4004141698745047040	4004029857796571136	5.104	5.100	14.09	16.07	0.00492	0.580	0.412	0.992	0.783
6779722291827283456	6779724009814201984	1.575	1.579	17.72	18.79	0.00712	0.484	0.378	0.862	0.641
3594791561220458496	3594797539814936832	1.065	1.069	14.44	16.31	0.0763	0.917	0.731	1.649	0.582
3871814958946253312	3871818601078520192	1.449	1.499	15.66	17.13	0.0188	0.676	0.657	1.333	0.533
2379971950014879360	2379995177198014976	1.604	1.588	14.21	16.58	0.0270	0.876	0.712	1.588	0.507
6826022069340212864	6826040868412655872	2.379	2.373	11.76	14.05	0.0987	1.016	0.738	1.754	0.572
5798275535462480768	5798276325736369024	1.247	1.261	13.32	13.76	0.000536	1.443	1.176	2.619	0.575

TABLE I: (Catalog I). High probability halo-like wide binaries with $a_{\perp} > 0.5$ pc and $M_T < 3 M_{\odot}$.

Source id1	Source id2	parallax1	parallax2	g mag1	g mag2	R chance align	M_1	M_2	M_T	a_{\perp} (pc)
2267239293401566464	2267227851609566336	2.672	2.572	12.29	19.33	0.000829	0.881	0.234	1.116	0.406
5398661947044908032	5398661642104481280	1.560	1.498	17.29	17.44	0.0887	0.585	0.605	1.191	0.488
5645583297690313600	5645583641287667072	1.600	1.516	15.76	17.49	0.00162	0.632	0.501	1.133	0.405
1455970587377673088	1455971102773749120	3.258	3.228	15.23	17.07	0.0424	0.647	0.478	1.125	0.311
1502056067500288000	1502056303722384896	1.360	1.434	17.88	19.17	0.0258	0.490	0.348	0.838	0.307
907782951948645120	907788037189915776	5.111	4.763	16.42	18.29	0.0139	0.415	0.242	0.656	0.310
2314269945503083136	2314271040719019520	2.865	2.957	15.56	18.54	4.05e-05	0.568	0.272	0.841	0.341
3572552289281102208	3572551876964275968	1.588	1.629	15.04	17.33	0.0701	0.687	0.513	1.200	0.336
1026212066635632896	1026210421663437056	3.098	2.999	16.30	16.70	0.00271	0.527	0.558	1.085	0.347
6490187654367322880	6490187826166014976	1.227	1.219	18.12	18.47	0.0233	0.626	0.491	1.117	0.373
2273522830556875008	2273522693118038528	2.250	2.181	18.26	19.21	0.000904	0.535	0.396	0.931	0.326
1233862465402949248	1233862121805561728	1.436	1.480	17.75	17.95	0.0695	0.550	0.529	1.078	0.375
1125577719872744576	1125601221933787904	2.168	2.267	16.60	17.99	0.0840	0.630	0.414	1.044	0.344
1893662595615946880	1893676545669800192	5.770	5.692	14.69	15.65	0.000329	0.636	0.513	1.149	0.472
4750157074016887168	4750145249971158400	1.516	1.482	17.24	17.45	7.73e-09	0.545	0.544	1.089	0.353
508745580667253888	508757396114325760	1.827	1.586	16.38	18.63	1.79e-09	0.734	0.394	1.129	0.311
2941779785735791744	2941779751375811456	1.782	1.678	17.03	17.22	0.0830	0.536	0.531	1.067	0.304
3167680015939190784	3167663626343991424	8.058	8.026	14.79	15.66	1.39e-05	0.418	0.366	0.784	0.339
2501107173271605120	2501154379256836992	2.279	2.189	13.94	17.58	0.0414	0.709	0.400	1.109	0.329
4709263174266830592	4709264411217678720	2.112	2.228	13.29	19.02	0.000916	0.826	0.251	1.077	0.338
744833091033565952	744832609997212288	3.231	3.314	16.31	17.64	3.49e-05	0.496	0.356	0.852	0.320
2226993972369172096	2226994526421033472	3.832	3.872	12.14	18.67	0.00108	0.820	0.207	1.027	0.305
5447292388566495104	5447291838810675072	3.118	3.176	17.14	17.66	0.0268	0.484	0.428	0.912	0.362
5563419473797009024	5563416377123646720	2.382	2.288	16.22	18.75	0.0161	0.634	0.400	1.034	0.337

TABLE II: (Catalog II). High probability wide binaries with $0.3 < a_{\perp} < 0.5$ pc and $M_T < 1.2 M_{\odot}$.

M_T	a_{\perp}
0.179	0.107
0.258	0.151
0.296	0.174
0.343	0.225
0.606	0.262
0.656	0.310
0.784	0.339
0.841	0.341
0.912	0.363
1.078	0.375
1.116	0.406
1.133	0.405
1.249	0.431
1.298	0.440
1.149	0.472
1.436	0.479
1.191	0.488

TABLE III: Candidates on the boundary with $0.1 < a_{\perp} < 0.5$ pc, representing the edge of the densely populated region.